Na2Fe(C2O4)F2: A new iron-based polyoxyanion cathode for Li/Na ion batteries

Wenjiao Yao,[†] Moulay-Tahar Sougrati,[§,‡] Khang Hoang,[¶] Jianing Hui,[†] Philip Lightfoot,[†,*] Anthony Robert Armstrong[†,‡*]

[†] School of Chemistry, University of St Andrews, St Andrews, Fife KY16 9ST, UK

[§]Université de Montpellier 2 Place Eugène Bataillon - CC 1502, 34095 Montpellier CEDEX 5, France

[¶] Center for Computationally Assisted Science and Technology, North Dakota State University, Fargo, ND 58108, USA

[‡]ALISTORE-ERI, 80039, Amiens Cedex, France

ABSTRACT: A new mixed anion compound, $Na_2Fe(C_2O_4)F_2$ has been prepared by hydrothermal synthesis. The crystal structure exhibits infinite chains of corner-linked Fe^{II}-centred octahedra, with coordination composed of both oxalate and fluoride ligands. This compound exhibits promising reversible lithium and sodium insertion. On extended cycling, $Na_2Fe(C_2O_4)F_2$ is capable of reversibly inserting 0.67 Li^+ or 0.56 Na^+ per formula unit up to 50 cycles at the average discharge voltages of 3.3 V and 3.0 V, respectively. This represents arguably the best performance as a prospective cathode material so far observed amongst oxalates, and is comparable to many known iron phosphate-based cathode materials.

I. INTRODUCTION

The ever increasing demand for portable energy has driven the search for new electrode materials for rechargeable battery applications. Until now lithium-ion batteries (LIBs) have been preferred to alternative chemistries as a result of their high energy density and operating voltages, but concerns surrounding Li supply and its rising cost have encouraged a rapidly growing interest in the more sustainable sodium-ion batteries (NIBs).[1-4] Until recently the latter have garnered little attention, providing many opportunities for the exploration of new electrode materials. Since sodium is highly abundant and therefore cheap, NIBs may find application in the grid storage sector, and could be major players in next-generation low-carbon energy technologies. Low cost and environmental impact are also strong drivers behind the search for new polyanion compounds using iron as a redox center.[5] The exploration of cathode materials for Na-ion batteries has encompassed layered transition metal (TM) oxides ($NaTMO_2$),[6] olivine-type ($NaTMPO_4$),[7-8] NASICON-type,[9-11] and a range of other polyoxyanionic structures (e.g. phosphates and sulfates).[12-20] The advantage of polyoxyanion-based compounds lies in their enhanced stability via strong covalent bonds, which in turn leads to improved safety characteristics. The incorporation of fluoride into polyoxyanionic systems is being widely investigated due to the opportunity to provide a tuneable potential owing to the larger ionicity of the TM-F bond compared with the corresponding TM-O bond. Examples include Na_2TMPO_4F, $NaVPO_4F$, $NaFeSO_4F$, etc.[21]

In the search for new iron-based cathode materials for either Li- or Na-ion batteries, we note that oxalic acid is a relatively strong acid, with acidity (pK_α = 1.25/4.14) between those of H_2SO_4 (pK_α = -3/1.99) and H_3PO_4 (pK_α = 2.15/7.20/12.32). This suggests that the electronic inductive effect of the oxalate group on the d-states of the transition metal ions should be similar to $(SO_4)^{2-}$ and $(PO_4)^{3-}$, and hence give rise to similar redox potentials to sulfate and phosphate. On the other hand, its conjugate base, $(C_2O_4)^{2-}$, is found to be a versatile anion since it may serve as a mono-dentate, bidentate, tridentate or tetradentate ligand and may form chains, layers, or three dimensional networks with metal centers.[22] Last, but not least, oxalic acid is a common starting material in synthetic chemistry, which is capable of both controlling the valence state of metals and acting as a template or mineralizer to facilitate crystal nucleation and growth.[23] So far, the exploration of oxalates as electrode materials is rare. Tarascon and co-workers have reported a few oxalate-based materials, with good performance obtained from $Fe_2(C_2O_4)_3 \cdot 4H_2O$.[24] This material shows a capacity of around 100 $mAhg^{-1}$ at an average potential of 3.3 V vs. Li^+/Li. It suffers from the drawback that it is fabricated in the charged state (Fe^{3+}), whereas positive electrodes are typically prepared in the discharged state (Fe^{2+}) and act as a lithium/sodium source for the negative electrode during battery operation. Also, the structural water molecules in $Fe_2(C_2O_4)_3 \cdot 4H_2O$ add extra mass, thereby limiting the practical capacity. The same research group also reported the sodium phases $Na_2M_2(C_2O_4)_3 \cdot 2H_2O$ (M = Fe, Mn, Co) but concluded that these materials showed limited electrochemical activity.[25] Yamada and co-workers reported that $K_4Na_2[Fe(C_2O_4)_2]_3 \cdot 2H_2O$ is electrochemically active but also with limited capacity.[26] No examples of iron fluoro-oxalate materials have been reported to date.

Inspired by these considerations, we have synthesized the first iron-based alkali fluoro-oxalate, formulated $Na_2Fe(C_2O_4)F_2$. Herein, we report hydrothermal synthesis, structural determination, physical characterization, and

primary electrochemical tests. The results showed that it could operate on the Fe^{2+}/Fe^{3+} couple, and exhibit promising reversible lithium and sodium insertion, and thus is promising to serve as an environmental friendly cathode material.

II. EXPERIMENTS

2.1 Synthesis

Single crystals of the title compound were synthesised by a hydrothermal method. Typically, as obtained $FeCl_2 \cdot 2H_2O$, $NaBF_4$, $H_2C_2O_4 \cdot 2H_2O$, Na_2CO_3 were mixed in a teflon-lined autoclave in the ratio of 1:3:3:4 (1 for 5 mmol), with 2 mL H_2O added as solvent. The autoclave was heated at 190°C for 4d and then cooled down in air. The synthesised product is a mixture of yellowish green crystals and colourless $NaBF_4$, which is highly soluble in water. The resulting products were repeatedly washed with distilled water and acetone and dried at 60°C. Similar procedures performed in the Co, Ni, Zn systems resulted in $NaCoF_3$, $NaNiF_3$, $NaZnF_3$, respectively. The Mn system gave rise to a totally different compound $Na_4Mn_4(C_2O_4)_5F_2 \cdot 4H_2O$, for which attempts to obtain pure sample are still ongoing.

2.2 Single crystal X-ray diffraction.

A yellowish green crystal was selected and mounted on nylon loops in inert oil and SXRD data were collected on a *Rigaku SCX Mini* diffractometer using Mo Kα radiation (λ = 0.710 73 Å) at 173 K. *Rigaku CrystalClear 2.0* was employed to index and process the data. The structure was then solved by direct methods and refined using SHELX-2014[27] incorporated in the WinGX program. Absorption corrections were performed semi-empirically from equivalent reflections on the basis of multi-scans. All atoms were refined anisotropically.

2.3 Characterization

The mid-infrared spectrum was obtained at room temperature using a Perkin Elmer Spectrum GX IR spectrometer. The spectra were collected in the range 400 to 4000 cm^{-1} with resolution of 1 cm^{-1}. PXRD patterns were recorded on a Stoe STADI/P diffractometer operating in transmission mode with Fe Kα_1 radiation (λ = 1.936 Å) in the 2θ range 10 °- 100 °, the total data collection time being 16 h. Data sets were refined by conventional Rietveld methods using the GSAS package with the EXPGUI interface.[28] The background, scale factor, zero point, lattice parameters and coefficients for the peak shape function were refined to convergence. Thermogravimetric analysis (TGA) was carried out with ground crystals of the title compound using a NETZSCH TG 209 thermal analyser. A sample (about 10 mg) of ground crystal was placed in an alumina crucible and heated from room temperature to 800°C at a rate of 5°C /min in flowing air atmosphere. The residues were examined and analysed by X-ray powder diffraction after the experiments. SEM images of prepared samples were taken on a JEOL JSM-6700F equipped with a field emission gun (FEG) electron source. Secondary electron images were recorded with a tungsten filament electron source using an accelerating voltage of 5 kV for the hand ground pristine sample, and 15 kV for ball-milled cathode samples. A retractable backscattered electron detector was applied for atomic number contrast imaging.

2.4 Electrochemistry

The material (0.3 g) was mixed with Super S carbon (0.15 g) for 30 min using a Fritsch Pulverisette 8 mill. Subsequently the powder was ground with binder (poltetrafluoroethylene, PTFE, 0.05g) until homogeneous. Typically, cathode pellets with 6-8 mg active material were tested in coin cells (CR2325, NRC Canada) with Li metal as anode, LP30 (1M $LiPF_6$ in ethylene carbonate: dimethyl carbonate = 1:1) as electrolyte for LIB, and Na metal as anode, 1 M $NaClO_4$ in propylene carbonate with 3% fluoroethylene carbonate as electrolyte for NIB. Half cells were then tested by galvanostatic cycling in the potential window 2.0-4.4 V for LIB, and 2.0-4.3 V for NIB at a rate of 10 mAg^{-1} using a Biologic Macpile II system. For samples prepared for Mössbauer spectroscopy, Kynar 2801 was used as binder instead of PTFE.

2.5 Mössbauer spectra

Room temperature Mössbauer spectra were recorded on absorbers prepared under argon (coffee-bags). Each absorber contains 30-40 mg/cm^2 active material recovered by washing with dimethyl carbonate (DMC). The spectrometer is operating in the constant acceleration transmission geometry. The γ-ray source (^{57}Co/Rd, 850 MBq) is maintained at room temperature. The isomer shift scale is calibrated using pure α-Fe standard. The obtained data are fitted using least-squares method and a combination of Lorentzian lines with MOSFIT program.

2.6 Calculations

The calculations were based on density-functional theory within the Perdew, Burke, and Ernzerhof[29] version of the generalized-gradient approximation and the projector-augmented wave method,[30, 31] as implemented in the Vienna Ab Initio Simulation Package (VASP).[32] The on-site Hubbard correction[33] with the effective U value of 4.0 eV was applied on the Fe 3d states and the van der Waals correction was taken into account using the approach of Grimme.[34] In all calculations, the energy cutoff was set at 500 eV and spin polarization was included.

III. RESULTS AND DISCUSSION

3.1 Structure

Pure samples were obtained *via* a mild hydrothermal method. The yellowish green crystals were easily detected by the naked eye. The crystallographic data determined from single crystal XRD on a 0.15×0.07×0.04 mm^3 crystal is displayed in Table 1. Atomic coordinates and selected bond lengths are shown in Tables S1-2. Figure 1 gives a graphic view of the structure. It clearly shows that the structure features zig-zag $[Fe(C_2O_4)F_2]^{2-}$ chains running along the *b*-axis. Within a $[Fe(C_2O_4)F_2]^{2-}$ chain, each Fe atom is coordinated by four coplanar O atoms from one bidentate and two mono-dentate oxalate moieties (d(Fe-O) = 2.1268(15) -2.2255(18) Å), and two *trans*-F atoms (d(Fe-F) = 1.9633(15)-1.9782(15) Å), forming a distorted, compressed octahedron. The adjacent $[FeO_4F_2]$ octahedra are

connected by sharing one O corner from an oxalate group and therefore form $[FeC_2O_4F_2]$ infinite chains. Each oxalate group connects three $[FeO_4F_2]$ octahedra, leaving one dangling oxygen atom. Notably, the Fe and oxalate group lie almost in the same plane, parallel to {2 0 1}, while the Fe-F bond is perpendicular to it. Two Na atoms located in the channel between the chains possess an open migration pathway along the *a*- and *b*- axes. Na1 is surrounded by four F atoms with bond lengths 2.2253(19) Å - 2.3490(16) Å and one O atom with bond length 2.2984(17) Å, while Na2 is coordinated to two F atoms (2.2624(17) Å – 2.2791(14) Å) and three O atoms (2.3404(20) Å - 2.5867(20) Å) (Figure S1). Bond Valence Sum (BVS)[35] calculations support the expected oxidation states (BVS values for Na1, Na2 and Fe of +1.104, +1.022 and +2.022, respectively).

Table 1 Crystallographic data for $Na_2Fe(C_2O_4)F_2$

Formula	$Na_2Fe(C_2O_4)F_2$
Crystal system	monoclinic
Space group	*C2/c (No. 15)*
a, *b*, *c* (Å)	15.8349(11), 5.9620(4), 12.2784(8)
β	111.968(7)
V(Å^3)	1075.01(14)
Z	8
F(000)	880
R (all data)	0.0298/0.0790
R *[I > 2σ(I)]*	0.0217/0.0692
Goodness-of-fit on F^2	0.0646

[a] $R(F) = \sum||F_o|-|F_c||/\sum|F_o|$ for $F_o^2 > 2\sigma(F_o^2)$.
[b] $R_w(F_o^2) = \{\sum[w(F_o^2-F_c^2)^2]/\sum wF_o^4\}^{1/2}$ for all data.

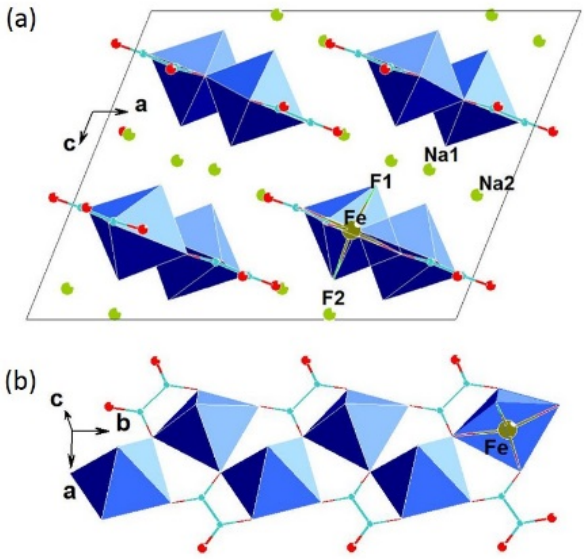

Figure 1. Crystal structure of $Na_2Fe(C_2O_4)F_2$. (a) unit cell viewed along the *b*-axis (b) $[Fe(C_2O_4)F_2]$ infinite chains. The FeO_4F_2 octahedra are shown in blue.

$Na_2Fe(C_2O_4)F_2$ crystallites obtained from the hydrothermal synthesis are predominantly in the size range 2-10 µm. A powder X-ray diffraction (PXRD) pattern of the hand ground material was recorded with Fe $K\alpha_1$ radiation (λ = 1.936 Å) to avoid Fe fluorescence. Rietveld analysis of the PXRD pattern confirmed the sample quality, with lattice parameters similar to those obtained from single-crystal analysis, as displayed in Figure 2. Only very minor peaks are observable from possible impurity phase(s). The hand ground sample shows an average size of 1-3 µm (Figure S2). No crystalline impurity could be detected. The presence of a small quantity of an amorphous impurity cannot be excluded since the Mössbauer spectrum of the pristine material (Figure 4d) is fitted with two contributions; the major one (green line, 90%) is assigned to iron(II) in an octahedral site in the crystalline $Na_2Fe(C_2O_4)F_2$ and a minor one (blue line, 10%) that could result from an amorphous iron(II) based impurity such as $Fe(C_2O_4)\cdot 2H_2O$. This contribution could also be explained by some structural defects as observed in lithium iron sulphates and lithium iron phosphates.[36, 37] It is worth noting that the main doublet shows a slight asymmetry that can be explained very likely by a preferred orientation as already observed in some sodium oxalates and malonates or a Goldanskii-Karyagin effect as reported for $Fe_3(CO)_{12}$.[25, 38]

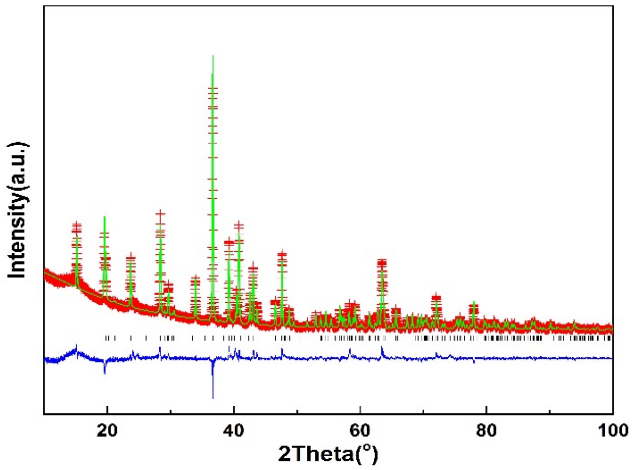

Figure 2. Rietveld analysis of hand-ground microcrystalline powder of synthesised sample. Lattice parameters in C 2/c are *a* = 15.8566(3) Å , *b* = 5.9645(1) Å , *c* = 12.3198(2) Å, *β* = 112.003(1). *wR*p = 0.0868, *R*p = 0.0678, χ^2 = 3.42.

3.2 Electrochemical properties

In order to compensate for the low electronic conductivity of the pure sample (Figure S3, Band gap ≈ 2.27 eV), the title compound was mixed with super S carbon in the weight ratio of 2:1 for 30 min using a Fritsch Pulverisette 8 mill. After ball milling with Super S carbon, the crystallite size is on average 100-500 nm, as displayed in Figure 3a-b. The Super S carbon is very well dispersed among the parent compound after ball milling and adheres to the surface of particles. Therefore the back scattered electron image (BSE) gives a clearer picture of the title compound than the secondary electron image (SE). This well dispersed mixture

also implies an improved conductivity within the composite electrode.

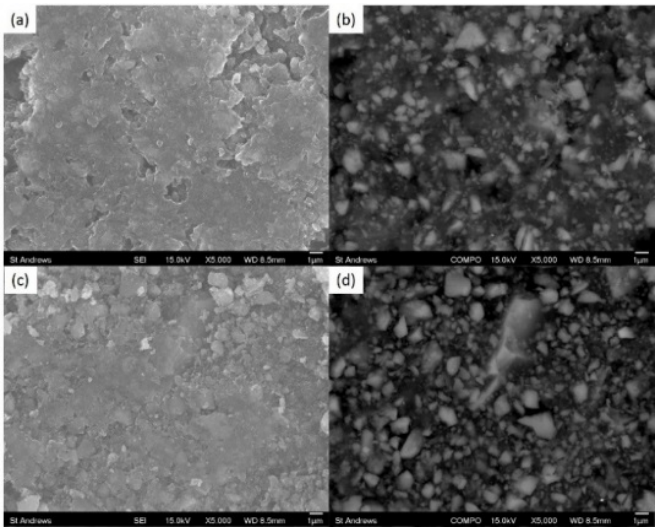

Figure 3. SEM image of cathode material in NIB (a-b) SE and BSE prepared as stated in the text (c-d) SE and BSE after 50 electrochemical cycles in the voltage window 2.0-4.3 V.

The electrochemical performance of $Na_2Fe(C_2O_4)F_2$ as a cathode in LIBs and NIBs was then evaluated galvanostatically in half cells using a Biologic Macpile II system. The typical loading of active material was 6-8 mg cm^{-2}. **Figure 4**a displays the voltage profiles of the first cycle at a rate of 10 mAg^{-1} (about C/12) in the voltage window of 2.0-4.4 V for LIB and 2.0-4.3 V for NIB. The charge-discharge profiles are both quite similar to the sloping curve observed on oxidation for Na_2FePO_4F.[12] The initial sodium extraction from $Na_2Fe(C_2O_4)F_2$ exhibits two plateaux, probably associated with structural phase transitions, with a step occurring at a composition of $Na_{1.5}Fe(C_2O_4)F_2$. The limit of sodium extraction corresponds to a composition of $NaFe(C_2O_4)F_2$. The two plateaux on the first charging curve are situated at 3.6 V and 3.9 V for LIB (Figure S4), and 3.3 V and 3.6 V for NIB (Figure 4b). An average difference of 0.3 V agrees well with the difference in electrochemical potential between Li and Na metal. Mössbauer spectra confirm the iron oxidation and reduction in the charge-discharge process, as indicated in Figure 4(d-f) and Table S3. The blue line shows the Fe^{2+} component (8%), which does not change during the cycling process. At 4.3 V charged state (Figure 4e), the spectrum is fitted with four doublets; the green and blue ones are the signature of a little amount of unreacted material due to the large amount of powder needed for ex situ analysis (40 mg/cm^2). The red and pink doublets are typical of iron(III) environments and represent 90% of the total iron at the charged state. This suggests that the $NaFe(C_2O_4)F_2$ phase has two crystallographic sites or some structural defects. In 2.0 V discharged state (Figure 4f), the

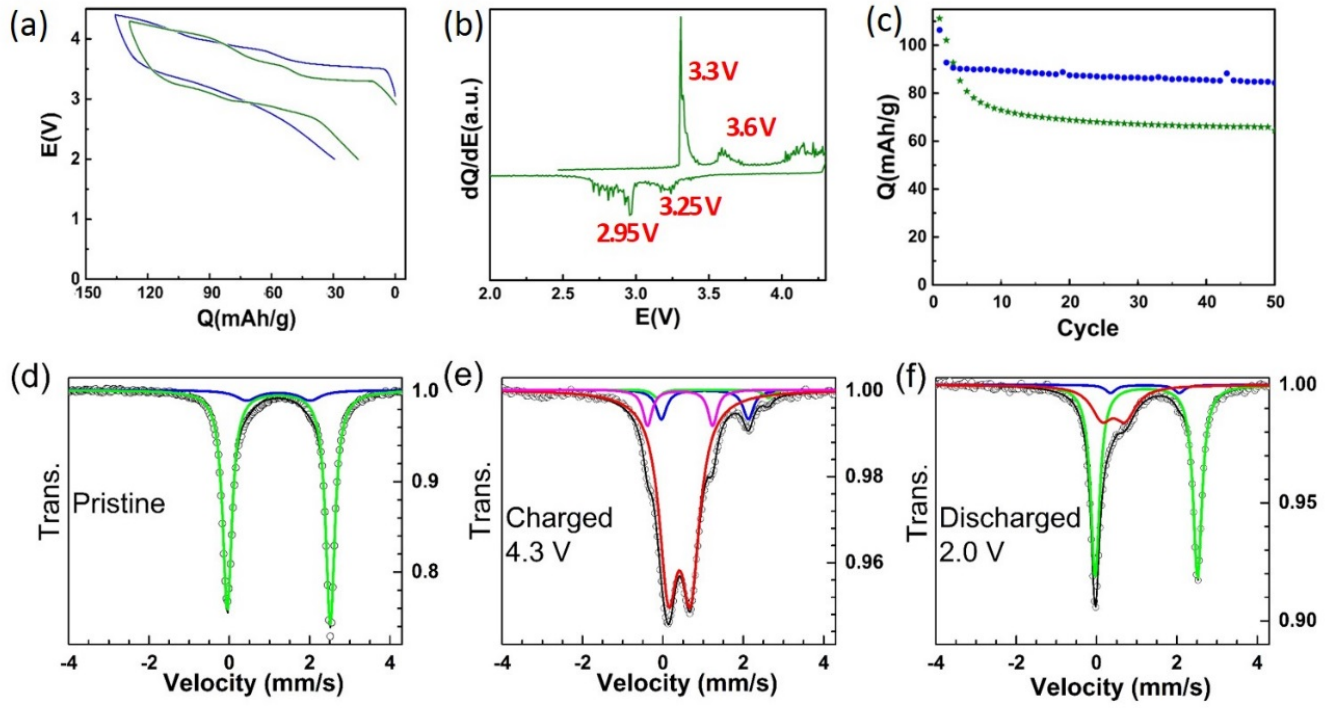

Figure 4. (a) Galvanostatic voltage profiles for $Na_2Fe(C_2O_4)F_2$ cathode in the voltage range of 2.0-4.4 V in LIB (blue), and 2.0-4.3 V in NIB (green) (b) dQ/dE curve of initial charge/discharge profiles in NIB. (c) Discharging capacity evolution for the first 50 cycles. Blue for LIB and green for NIB. Mössbauer spectra of $Na_2Fe(C_2O_4)F_2$ in (d) pristine cathode; (e) charged to 4.3V state; (f) discharged to 2.0 V. Observed and calculated patterns are present as black circles and lines, respectively. The blue, green, red and pink lines are described in the text.

spectrum mainly consists of Fe^{2+}, with some unreduced Fe^{3+} suggesting an incomplete reduction at this voltage. This is in good agreement with the irreversible capacity. The large cell polarization probably arises from the conductivity of the pristine material. The capacity faded over the first few cycles (**Figure 5**), and then stabilized at around 90 $mAhg^{-1}$ at an average discharge potential of 3.3 V for $Na_{2-x}Li_xFe(C_2O_4)F_2$, and 70 $mAhg^{-1}$ at an average discharge potential of 3.0 V for $Na_2Fe(C_2O_4)F_2$ as shown in Figure 4c. The capacity fading might arise from a little overcharge that cause irreversible structure change as indicated by the little convex after 4.0 V in Figure 4b, and incomplete reduction at 2.0 V as proved by Mössbauer spectrum (Figure 4f). After 50 cycles, the recovered cathode of NIB showed no change in morphology (Figure 3c-d). It is worth noting that almost 100% of the theoretical capacity (133 $mAhg^{-1}$ for LIB and 124 $mAhg^{-1}$ for NIB) was extracted on the first charge of both cells.

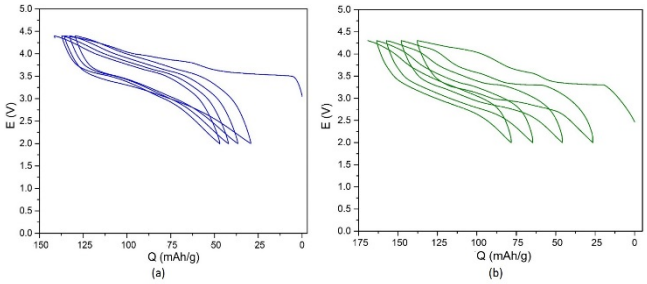

Figure 5. The first five cycles of the LIB (a) and NIB (b) using carbon-coated $Na_2Fe(C_2O_4)F_2$ cathode.

3.3 Calculations

First-principles calculations were further carried out to elucidate the mechanism of electrochemical activity. We find that the iron ion in $Na_2Fe(C_2O_4)F_2$ is stable as high-spin Fe^{2+} with a calculated magnetic moment of 3.77 μB, in perfect agreement with the Mössbauer isomer shift. The antiferromagnetic and ferromagnetic spin configurations of the iron array are degenerate in energy. **Figure 6** shows the total and projected electronic density of states of $Na_2Fe(C_2O_4)F_2$. The compound has a calculated band gap of 1.94 eV, which is in reasonable agreement with the experimental value. The gap is indirect with the valence-band maximum at the Γ point and the conduction-band maximum at the Z point in the Brillouin zone. It can be seen from Figure 6 that the top of the valence band is predominantly composed of Fe 3d states. As the extraction of Na from the NIB cathode involves removing one electron from the valence-band top, the electronic structure indicates that the intrinsic extraction/(re)-insertion mechanism involves Fe^{3+}/Fe^{2+} redox. Indeed, we find that Fe^{2+} is oxidized into Fe^{3+} upon Na removal; the calculated magnetic moment of high-spin Fe^{3+} is 4.33μ_B. The average redox potential is 3.54 V vs Na between $Na_2Fe(C_2O_4)F_2$ and $NaFe(C_2O_4)F_2$, which is in good agreement with the average experimental value during first charge (Figure 4b and e).

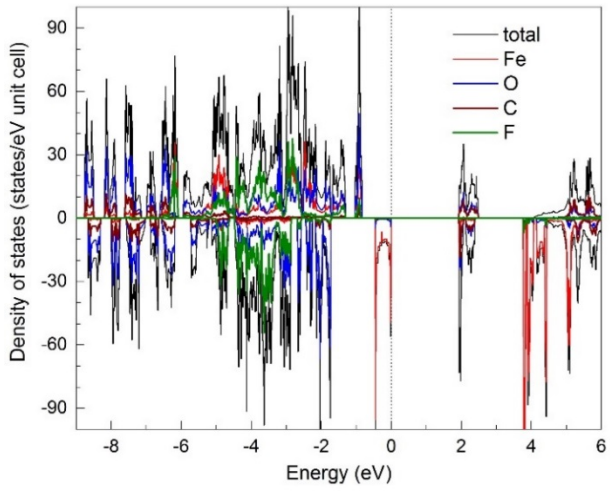

Figure 6. Total and projected electronic density of states of $Na_2Fe(C_2O_4)F_2$. The zero of the energy (at 0 eV) is set to the highest occupied state.

3.4 Further characterization

IR spectroscopy was carried out with the objective of determining the coordination of atoms in the sample and to confirm the absence of incorporation of H_2O or OH^-. In **Figure 7**a, there are no absorption peaks in the range of 3000-4000 cm^{-1}, verifying no H_2O or OH^- in the obtained sample. The detailed assignment of absorption peaks is stated in *Supporting Information*. $Na_2Fe(C_2O_4)F_2$ is thermally stable up to 267°C in air, before gradual weight loss occurs with complete decomposition to NaF and Fe_2O_3 occurring above 410°C (Figure 7b). This is stable enough for normal working environments. On immersion in water, it undergoes a slow reaction to form $Fe(C_2O_4)\cdot 4H_2O$, as indicated in Figure S5. The synthesis of the lithium analogue of $Na_2Fe(C_2O_4)F_2$ was attempted via a topotactic ion-exchange of the Na for Li by refluxing in excess LiBr/LiCl in CH_3CN or N-Methyl-2-pyrrolidone. Although $Na_2Fe(C_2O_4)F_2$ is quite stable in pure solvent, addition of LiBr/LiCl produced a yellow solution, which indicated the dissolution of Fe^{2+}. After total evaporation of the solvent, the residue contained amorphous Fe_2O_3 and LiF (Figure S6).

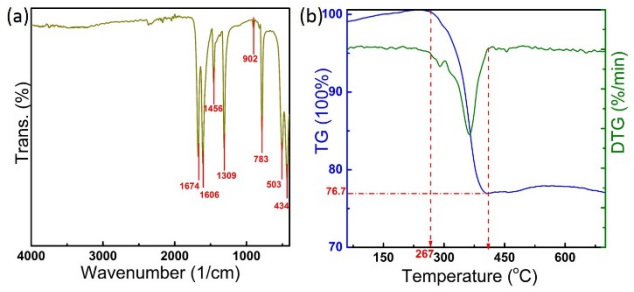

Figure 7. IR spectrum(a) and TG(b) of $Na_2Fe(C_2O_4)F_2$

IV. CONCLUSION

In conclusion, a Fe-based polyoxyanion material $Na_2Fe(C_2O_4)F_2$ was prepared through hydrothermal synthesis. It is the first fluoro-oxalate cathode material re-

ported to date. The structure was determined through single crystal X-ray diffraction. Electrochemical tests reveal that almost 100% of the theoretical capacity (133 mAh/g for LIB and 124 mAh/g for NIB) was extracted on the first charge at an average voltage of 3.6 V and 3.3 V, respectively. On extended cycling, $Na_2Fe(C_2O_4)F_2$ is capable of reversibly inserting 0.67 Li^+ or 0.56 Na^+ per unit formula unit up to 50 cycles in the present work, but might be improved with optimized condition, such as changing voltage window. This represents arguably the best oxalate positive electrode material reported to date, with comparable performance to $Fe_2(C_2O_4)_3 \cdot 4H_2O$ but with the advantage that it is fabricated in the discharged state. In addition, replacing or doping Fe with Mn or other multi-valent state ions is beneficial for a higher redox potential as well as a higher capacity in this system. The present study of $Na_2Fe(C_2O_4)F_2$ confirms that oxalates represent a promising class of polyoxyanion positive electrode materials. It appears that oxalates display discharge voltages lower than those of sulfates but comparable to those of phosphates, which reflects the electronegativity of $(SO_4)^{2-} > (C_2O_4)^{2-} > (PO_4)^{3-}$. Further research on oxalates may give rise to even more interesting potential electrode materials.

ASSOCIATED CONTENT

Supporting Information. Atomic coordinates, selected bond length, assignment of IR spectroscopy, UV-Vis Absorption Spectrum, and crystal information file (CIF) are attached as the supporting files. This material is available free of charge via the Internet at http://pubs.acs.org.

AUTHOR INFORMATION

Corresponding Author

*pl@st-andrews.ac.uk (PL); *ara@st-andrews.ac.uk(ARA)

Author Contributions

The manuscript was written through contributions of all authors. All authors have given approval to the final version of the manuscript.

ACKNOWLEDGMENT

Thanks to Mr. Pifu Gong and Prof. Zheshuai Lin (Technical Institute of Physics and Chemistry, Chinese Academy of Sciences) for helpful discussions. Thanks to Prof. John T. S. Irvine and Dr. Paul Connor (School of Chemistry, University of St Andrews) for electrochemical test support. W.Y. thanks the Royal Society for the award of a Newton International Fellowship (140881). Work at North Dakota State University (NDSU) was supported by the U.S. Department of Energy Grant No. DE-SC0001717 and by NDSU's Center for Computationally Assisted Science and Technology.

REFERENCES

[1] Tarascon, J. M.; Armand, M. Issues and challenges facing rechargeable lithium batteries. *Nature* **2001**, *414*, 359-367.

[2] Palomares, V.; Cabanas, M. C.; Martinez, E. C.; Han, M. H.; Rojo, T. Update on Na-based battery materials. A growing research path. *Energy Environ. Sci.* **2013**, *6*, 2312–2337.

[3] Larcher, D.; Tarascon, J. M. Towards greener and more sustainable batteries for electrical energy storage. *Nature Chem.* **2015**, *7*, 19–29.

[4] Yabuuchi, N.; Kubota, K.; Dahbi, M.; Komaba, S. Research development on sodium-ion batteries. *Chem. Rev.* **2014**, *114*, 11636–11682.

[5] Pan, H. L.; Hu, Y. S.; Chen, L. Q. Room-temperature stationary sodium-ion batteries for large-scale electric energy storage. *Energy Environ. Sci.* **2013**, *6*, 2338-2360.

[6] Han, M. H.; Gonzalo, E.; Singh, G.; Rojo, T. A comprehensive review of sodium layered oxides: powerful cathodes for Na-ion batteries. *Energy Environ. Sci.* **2015**, *8*, 81-122.

[7] Moreau, P.; Guyomard, D.; Gaubicher, J.; Boucher, F. Structure and stability of sodium intercalated phases in olivine $FePO_4$. *Chem. Mater.* **2010**, *22* (14), 4126–4128.

[8] Lee, K. T.; Ramesh, T. N.; Nan, F.; Botton, G. and Nazar, L. F. Topochemical synthesis of sodium metal phosphate olivines for sodium-ion batteries. *Chem. Mater.* **2011**, *23*, 3593–3600.

[9] Jian, Z. L.; Yuan, C. C.; Han, W. Z.; Lu, X.; Gu, L.; Xi, X. K.; Hu, Y. S.; Li, H.; Chen, W.; Chen , D. F.; Ikuhara, Y.; Chen, L. Q. Atomic structure and kinetics of NASICON $Na_xV_2(PO_4)_3$ cathode for sodium-ion batteries. *Adv. Funct. Mater.* **2014**, *24*, 4265–4272.

[10] Anantharamulu, N.; Koteswara, R.K.; Rambabu, G.; Vijaya, K.B., Radha, V. and Vithal, M. A wide-ranging review on Nasicon type materials. *J. Mater. Sci.* **2011**, *46*, 2821–2837.

[11] Chakir, M.; El Jazouli, A. and Waal, D. Synthesis, crystal structure and spectroscopy properties of $Na_3AZr(PO_4)_3$ (A=Mg, Ni) and $Li_{2.6}Na_{0.4}NiZr(PO4)_3$ phosphates. *J. Solid State Chem.* **2006**, *179*, 1883–1891.

[12] Ellis, B. L.; Makahnouk, W. R. M.; Makimura, Y.; Toghill, K.; Nazar, L. F. A multifunctional 3.5 V iron-based phosphate cathode for rechargeable batteries. *Nature Mater.* **2007**, *6*, 749-755.

[13] Recham, N.; Chotard, J. N.; Dupont, L.; Djellab, K.; Armand, M.; Tarascon, J. M. Ionothermal synthesis of sodium-based fluorophosphate cathode materials. *J. Electrochem. Soc.* **2009**, *156* (12), A993-A999.

[14] Ellis, B. L.; Makahnouk, W. R. M.; Weetaluktuk, W. N. R.; Ryan, D. H.; Nazar, L. F. Crystal structure and electrochemical properties of A_2MPO_4F fluorophosphates (A = Na, Li; M = Fe, Mn, Co, Ni). *Chem. Meter.* **2010**, *22*, 1059-1070.

[15] Kim, H.; Park, I.; Seo, D. H.; Lee, S.; Kim, S. W.; Kwon, W. J.; Park, Y. U.; Kim, C. S.; Jeon, S.; Kang, K. New iron-based mixed-polyanion cathodes for lithium and sodium rechargeable batteries: combined first principles calculations and experimental study. *J. Am. Chem. Soc.* **2012**, *134*, 10369–10372.

[16] Barpanda, P.; Ati, M.; Melot, B. C.; Rousse, G.; Chotard, J. N.; Doublet, M. L.; Sougrati, M. T., Corr, S. A.; Jumas, J. C.; Tarascon, J. M. A 3.90V iron-based fluorosulphate material for lithium-ion batteries crystallizing in the triplite structure. *Nature Mater.* **2011**, *10*, 772-779.

[17] Recham, N.; Rousse, G.; Sougrati, M. T.; Chotard, J. N.; Frayret, C.; Mariyappan, S., Melot, B. C.; Jumas, J. C.; Tarascon, J. M. Preparation and characterization of a stable $FeSO4F^-$based framework for alkali ion insertion electrodes. *Chem. Mater.* **2012**, *24*, 4363–4370.

[18] Barpanda, P.; Oyama G.; Nishimura, S.; Chung S. C.; Yamada, A. A 3.8-V earth-abundant sodium battery electrode. *Nat. Commu.* **2014**, *5*, 4358-4365.

[19] Ati, M.; Dupont, L.; Recham, N.; Chotard, J.N.; Walker, W.T.; Davoisne, C.; Barpanda, P.; Sarou-Kanian, V., Armand, M.; Tarascon, J.M. Synthesis, structural, and transport properties of novel bihydrated fluorosulphates $NaMSO_4F_3 \cdot 2H_2O$(M=Fe, Co, and Ni). *Chem. Mater.* **2010**, *22*, 4062–4068.

[20] Barpanda, P.; Chotard, J. N.; Recham, N.; Delacourt, C.; Ati, M.; Dupont, L.; Armand M.; Tarascon, J. M. Structural, transport, and electrochemical investigation of novel $AMSO_4F$ (A

= Na, Li; M = Fe, Co, Ni, Mn) metal fluorosulphates prepared using low temperature synthesis routes. *Inorg. Chem.* **2010**, *49*, 7401–7413.

[21] Masquelier, C.; Croguennec, L. Polyanionic (phosphates, silicates, sulfates) frameworks as electrode materials for rechargeable Li (or Na) batteries. *Chem. Rev.* **2013**, *113*, 6552–6591.

[22] Abeysinghe, D.; Smith, M. D.; Yeon, J.; Morrison, G.; Loye, H. C. Z. Observation of multiple crystal-to-crystal transitions in a new reduced vanadium oxalate hybrid material, $Ba_3[(VO)_2(C_2O_4)_5(H_2O)_6]\cdot(H_2O)_3$, prepared via a mild, two-step hydrothermal method. *Cryst. Growth Des*. **2014**, *14*, 4749–4758.

[23] Yang, S. H.; Li, G. B.; Tian, S. J.; Liao, F. H.; Lin, J. H. Synthesis, structure, and magnetic properties of hydroxo-bridged vanadium oxalate $V_2O_2(OH)_2(C_2O_4)(H_2O)_2$. *Eur. J. Inorg. Chem.* **2006**, *14*, 2850–2854.

[24] Ahouari, H.; Rousse, G.; Carvajal, J. R.; Sougrati, M. T.; Saubanère, M.; Courty, M.; Recham, N.; Tarascon, J. M. Unraveling the structure of iron(III) oxalate tetrahydrate and its reversible Li insertion capability. *Chem. Mater.* **2015**, *27*, 1631–1639.

[25] Ahouari, H.; Rousse, G.; Klein, Y.; Chotard, J. N.; Sougrati, M. T.; Recham, N.; Tarascon, J. M. Synthesis, structure & electrochemical properties of metal malonate $Na_2M(H_2C_3O_4)_2\cdot nH_2O$ (n=0, 2) compounds and comparison with oxalate $Na_2M_2(C_2O_4)_3\cdot 2H_2O$ compounds. *Solid State Sci.* **2015**, *42*, 6-13.

[26] Wang, X. F.; Kurono, R.; Nishimura, S.; Okubo, M.; Yamada, A. Iron–oxalato framework with one-dimensional open channels for electrochemical sodium-ion intercalation. *Chem. Eur. J.* **2015**, *21*, 1096–1101.

[27] Sheldrick, G. M. *SHELXL-2014*, Program for the Refinement of Crystal Structures University of Göttingen, Göttingen, Germany, **2014**.

[28] Toby, B. H. EXPGUI, a graphical user interface for GSAS. *J. Appl. Crystallogr.* **2001**, *34*, 210–213.

[29]Perdew, J. P.; Burke, K.; Ernzerhof, M. Generalized gradient approximation made simple. *Phys. Rev. Lett*. **1996**, *77*, 3865-3858.

[30] Blochl, P. E. Projector augmented-wave method. *Phys. Rev. B* **1994**, 50, 17953-17979.

[31] Kresse, G.; Joubert, D. From ultrasoft pseudopotentials to the projector augmented-wave method. *Phys. Rev. B* **1999**, *59*, 1758-1775.

[32] Kresse, G.; Furthmüller, J. Efficiency of ab-initio total energy calculations for metals and semiconductors using a plane-wave basis set. *Comput. Mat. Sci.* **1996**, *6*, 15-50.

[33] Dudarev, S. L.; Botton, G. A.; Savrasov, S. Y.; Humphreys, C. J.; Sutton, A. P. Electron-energy-loss spectra and the structural stability of nickel oxide: An LSDA+U study. *Phys. Rev. B* **1998**, *57*, 1505-1509.

[34] Grimme, S. Semiempirical GGA-type density functional constructed with a long-range dispersion correction. *J. Comp. Chem*. **2006**, *27*, 1787-1799.

[35] Brese, N. E.; O' Keeffe, M. Bond-valence parameters for solids. *Acta Cryst.* **1991**, *B47*, 192-197.

[36] Lander, L.; Reynaud, M.; Rousse, G.; Sougrati, M. T.; Laberty-Robert, C.; Messinger, R. J.; Deschamps, M.; Tarascon J.-M. Synthesis and electrochemical performance of the orthorhombic $Li_2Fe(SO_4)_2$ polymorph for Li-ion batteries. *Chem. Mater.* **2014**, *26*, 4178–4189.

[37] Amisse, R.; Sougrati, M. T.; Stievano, L.; Davoisine,; C. Dražič, G.; Budič, B.; Dominko, R.; Masquelier, C. Singular structural and electrochemical properties in highly defective "$LiFePO_4$" powders. *Chem. Mater.*, **2015**, *27*, 4261–4273.

[38] Grandjean, F.; Long, G. J.; Benson, C. G.; Russo, U. Goldanskii-Karyagin asymmetry in $Fe_3(CO)_{12}$, *Hyperfine Interactions*, **1988**, *40*, 299-302.

Table of Contents (TOC)